The Astrophysical Journal, 972:103 (14pp), 2024 September 1 https://doi.org/10.3847/1538-4357/ad630b

ϵ Sagittarii: An Extreme Rapid Rotator with a Decretion Disk

Jeremy Bailey[1], Fiona Lewis[1], Ian D. Howarth[2], Daniel V. Cotton[3,4], Jonathan P. Marshall[5], and Lucyna Kedziora-Chudczer[6]
[1] School of Physics, University of New South Wales, Sydney, NSW 2052, Australia; j.bailey@unsw.edu.au
[2] University College London, Gower Street, London, WC1E 6BT, UK
[3] Monterey Institute for Research in Astronomy, 200 Eighth Street, Marina, CA 93933, USA
[4] Western Sydney University, Locked Bag 1797, Penrith-South DC, NSW 1797, Australia
[5] Institute of Astronomy and Astrophysics, Academia Sinica, 11F of AS/NTU, Astronomy-Mathematics Building, No.1, Sec. 4, Roosevelt Road, Taipei 106216, Taiwan
[6] Centre for Astrophysics, University of Southern Queensland, Toowoomba, QLD 4350, Australia
Received 2024 May 23; revised 2024 July 8; accepted 2024 July 8; published 2024 August 28

Abstract

We report high-precision, multiwavelength linear-polarization observations of the bright B9 (or A0) star ϵ Sagittarii. The polarization shows the distinctive wavelength dependence expected for a rapidly rotating star. Analysis of the polarization data reveals an angular rotation rate ω ($=\Omega/\Omega_{\rm crit}$) of 0.995 or greater, the highest yet measured for a star in our Galaxy. An additional wavelength-independent polarization component is attributed to electron scattering in a low-density, edge-on gas disk that also produces the narrow absorption components seen in the spectrum. Several properties of the star (polarization due to a disk, occasional weak Hα emission, and multiple periodicities seen in space photometry) resemble those of Be stars, but the level of activity in all cases is much lower than that of typical Be stars. The stellar properties are inconsistent with single-rotating-star evolutionary tracks, indicating that it is most likely a product of binary interaction. The star is an excellent candidate for observation by interferometry, optical spectropolarimetry to detect the Öhman effect, and ultraviolet polarimetry, any of which would allow its extreme rotation to be tested and its stellar properties to be refined.

Unified Astronomy Thesaurus concepts: Polarimetry (1278); Stellar rotation (1629); Circumstellar disks (235)

1. Introduction

The nonspherical shape of a rapidly rotating star results in a net linear polarization of the integrated light of the star. This effect was first predicted by Harrington & Collins (1968), but the resulting polarizations are small, and have only recently been observed (Cotton et al. 2017a; Bailey et al. 2020a; Lewis et al. 2022; Howarth et al. 2023). The polarization has a distinctive wavelength dependence, and is strongly dependent on the rotation rate ω, the axial inclination, and the gravity of the star. This allows polarization data, combined with other observations, to set significant constraints on the stellar properties.

ϵ Sagittarii (HD 169022, hereafter ϵ Sgr) is a bright ($V = 1.85$), rapidly rotating star at a distance of 44 pc (van Leeuwen 2007) and with a number of anomalous properties. The spectral type is variously reported as B9 IVp (Slettebak 1975), B9.5 III (Houk 1982), A0 II (Gray & Garrison 1987), and A0 III (Paunzen et al. 2001). Narrow, "shell" absorption components in the Balmer and other lines are seen (Slettebak 1975), and Gray & Garrison (1987) call it a "proto-shell star." It has been suggested to be a λ Boo star (Slettebak 1975). However, Baschek & Slettebak (1988) conclude, from a detailed abundance study, that ϵ Sgr, while "peculiar in both spectrum and colors, is definitely not a λ Boo star."

A companion star of magnitude $V \sim 7.7$ at a distance of $\sim 2.1''$ was discovered by Golimowski et al. (1993). Infrared (IR) observations by Hubrig et al. (2001) give the K magnitude of the companion as 6.5, and are consistent with it being a main-sequence star of 0.95 $M_\odot$ with $T_{\rm eff} = 5808$ K.

ϵ Sgr was found to have an IR excess in 60 μm Infra Red Astronomical Satellite (IRAS) data by Cote (1987). The IRAS excess was interpreted by Rhee et al. (2007) as originating from a dust disk with a temperature of 100 K at a radius of $3.5''$ from the star (equivalent to 150 au) and a fractional luminosity ($L_{\rm dust}/L_\star = 4.46 \times 10^{-6}$). The IR excess was also detected by Spitzer at 13 and 31 μm (Chen et al. 2014).

Polarization observations of ϵ Sgr were reported by Cotton et al. (2016a) and Bailey et al. (2017), and were larger than expected at its distance, implying the presence of intrinsic polarization. In this paper, we report a more extensive set of polarization observations and compare these with models of rapidly rotating stars.

2. Observations

2.1. Polarization Measurements

We report here 28 linear-polarization observations of ϵ Sgr. Of these, 26 were made on the 3.9 m Anglo-Australian Telescope (AAT) at Siding Spring Observatory using either the High-Precision Polarimetric Instrument (HIPPI; Bailey et al. 2015) or HIPPI-2 (Bailey et al. 2020b) polarimeters. Two observations were made with the Mini-HIPPI (Bailey et al. 2017) polarimeter on the 35 cm telescope at the University of New South Wales observatory in Sydney. These three polarimeters all use similar techniques, making use of ferro-electric liquid-crystal modulators operating at 500 Hz, and compact photomultiplier tubes as detectors. Some of the observations were previously reported by Cotton et al. (2016a) and Bailey et al. (2017), but all the data presented here have been reanalyzed using the methods described by Bailey et al. (2020b). We adopt a new calibration of modulator performance that has been carried out for an upcoming paper

Table 1
Summary of Observing Runs and Telescope Polarization Calibrations

Run	Date Range[d] (UT)	Telescope and Instrument Setup[a]							Observations[b]			Calibration[c]	
		Instr.	Tel.	$f/$	Ap. (arcsec)	Mod.	Filt.	Det.[e]	n	$\lambda_{\rm eff}$ (nm)	Eff. (%)	$q_{\rm TP}$ (ppm)	$u_{\rm TP}$ (ppm)
2014AUG	2014-09-01	HIPPI	AAT	8	6.6	BNS-E1	g'	B	1	463.1	89.0	-39.9 ± 0.9	-38.2 ± 0.9
2016FEB/JUN[f]	2016-02-27 to 06-25	HIPPI	AAT	8	6.6	BNS-E2	g'	B	2	463.8	86.9	-20.5 ± 1.7	4.5 ± 1.8
							r'	R	1	619.9	80.6	-8.2 ± 1.7	1.3 ± 1.7
m2016JUN	2016-06-10	M-HIPPI	UNSW	11	58.9	MT	Clear	B	1	467.9	75.5	-64.5 ± 4.3	-7.6 ± 4.4
m2016JUL	2016-08-31	M-HIPPI	UNSW	11	58.9	MT	Clear	B	1	464.0	74.3	-74.5 ± 3.1	-11.7 ± 3.1
2017JUN	2017-06-26 to 07-04	HIPPI	AAT	8	6.6	BNS-E2	425SP	B	1	400.1	49.4	-7.6 ± 3.8	8.8 ± 3.8
							g'	B	1	463.3	86.8	-9.1 ± 1.5	-2.6 ± 1.4
							650LP	R	1	717.6	62.7	-8.6 ± 2.5	-5.3 ± 2.5
2017AUG	2017-08-08 to 08-14	HIPPI	AAT	8	6.6	BNS-E2	425SP	B	1	400.2	49.5	-7.6 ± 3.8	8.8 ± 3.8
							500SP	B	1	435.3	74.0	-10.0 ± 1.7	-0.4 ± 1.6
							r'	R	2	619.2	80.7	-10.6 ± 1.3	-7.1 ± 1.3
2018MAR	2018-03-18 to 04-06	HIPPI-2	AAT	8[g]	25.5	BNS-E3	g'	B	2	461.7	81.5	128.1 ± 0.9	3.8 ± 0.9
							r'	R	2	620.9	84.5	109.1 ± 1.4	6.9 ± 1.4
2018JUL[h]	2018-07-12 to 07-25	HIPPI-2	AAT	8[g]	11.9	BNS-E4	V	B	1	532.3	96.6	-20.1 ± 1.5	2.3 ± 1.5
							r'	B	1	602.0	88.9	-10.3 ± 2.2	3.6 ± 2.2
2018AUG[h]	2018-08-21 to 09-01	HIPPI-2	AAT	8[g]	11.9	BNS-E5	500SP	B	1	438.2	55.1	1.9 ± 1.4	18.0 ± 1.4
							V	B	1	532.4	95.7	-20.1 ± 1.5	2.3 ± 1.5
							650LP	R	1	720.9	76.8	-6.5 ± 1.8	3.8 ± 1.8
2023APR/MAY[i]	2023-06-03	HIPPI-2	AAT	15	12.7	ML-E1	425SP	B	1	398.8	79.3	-1.0 ± 2.4	7.8 ± 2.1
							500SP	B	1	438.2	86.9	-20.1 ± 1.7	-5.1 ± 1.5
							g'	B	1	460.2	89.2	5.9 ± 1.0	0.0 ± 1.0
							r'	B	1	601.8	64.2	4.9 ± 4.5	-19.7 ± 3.9
							r'	R	1	620.8	60.5	-2.7 ± 3.2	-18.8 ± 3.3
							650LP	R	1	719.1	44.6	-36.6 ± 5.8	-35.4 ± 6.2

Notes.
[a] A full description, along with transmission curves for all the components and modulation characterization of each modulator ("Mod.") in the specified performance era, can be found in Bailey et al. (2020b).
[b] Mean values are given as representative of the observations made of ϵ Sgr. Individual values are given in Table 2 for each observation; n is the number of observations of ϵ Sgr.
[c] Most of the observations used to determine the telescope polarization (TP) and the high-polarization standards observed to calibrate position angle (PA) are described in Bailey et al. (2017, m2016JUN, m2016JUL), Bailey et al. (2015, 2014MAY), Cotton et al. (2017b, 2016FEB, 2016JUN), Cotton et al. (2019, 2017JUN, 2017AUG), and Bailey et al. (2020b, other runs). These are the first data presented from the 2023MAY run; 2–6 total observations per band of HD 2151, HD 61421, HD 102647, HD 102870, or HD 140573 were used to determine TP; PA was calibrated with reference to HD 84810, HD 161471, HD 111613, and HD 183143.
[d] Dates given are for observations of ϵ Sgr and/or control stars.
[e] B and R indicate blue- and red-sensitive H10720-210 and H10720-20 photomultiplier-tube detectors, respectively.
[f] TP calibration was carried out using observations combined from the 2016FEB and 2016JUN runs.
[g] Indicates use of a 2× negative achromatic lens, effectively making the foci $f/16$.
[h] TP calibration was carried out using observations combined from the 2018JUL and 2018AUG runs.
[i] TP calibration was carried out using observations combined from the 2023APR A/B and 2023MAY runs.

(D. V. Cotton et al. 2024, in preparation). The resulting final polarization values are similar to past work.

Details of the observing runs, made between 2014 and 2023, as well as instrumental details are listed in Table 1. The polarization observations of ϵ Sgr are listed in Table 2. New observations of interstellar control stars are described in the Appendix. The AAT observations were obtained with a range of broadband filters. The Sloan Digital Sky Survey (SDSS) g' and r' filters used with HIPPI were made by Omega Optics. For HIPPI-2, the corresponding filters were Generation 2 filters from Astrodon Photometrics. The two Mini-HIPPI observations were made with no filter ("Clear"). A bandpass model as described in Bailey et al. (2020b) was used to determine the effective wavelength and modulation efficiency for each observation. This model takes account of all the optical components as well as the source spectrum and atmospheric transmission. These values are listed in Table 2, and the effective wavelengths for these observations range from ∼400 to ∼720 nm.

2.2. Imaging

Infrared images of ϵ Sgr were obtained on 2016 September 10 using the IRIS2 instrument (Tinney et al. 2004) on the 3.9 m AAT in a narrowband filter at a wavelength of 2.3 μm. The separation (ρ) and position angle of the companion were measured from the images with the Python `Photutils` package (Bradley et al. 2022) using profile-fitting methods based on the DAOPHOT algorithms (Stetson 1987). The results, together with those from past observations, are listed in Table 3. The separation of the companion has been slowly increasing, with little change to the position angle.

The companion was included in the aperture for all our polarization observations. However, it contributes less than 1% of the optical-region light, and as a main-sequence G star is not

Table 2
Polarization Observations of ϵ Sgr (Sorted by Effective Wavelength)

Run	UT (Mid-point)	Dwell (s)	Exp. (s)	Filt.	Det.[a]	$\lambda_{\rm eff}$ (nm)	Eff. (%)	q (ppm)	u (ppm)	p (ppm)	θ (deg)
2023MAY	2023-06-03 16:39:20	1615	1280	425SP	*B*	398.8	79.3	-5.8 ± 12.1	-13.6 ± 12.0	14.8 ± 12.0	123.6 ± 27.9
2017JUN	2017-06-26 16:29:55	1557	800	425SP	*B*	400.1	49.4	6.7 ± 15.6	-50.3 ± 15.6	50.7 ± 15.6	138.8 ± 9.2
2017AUG	2017-08-10 14:14:07	2124	800	425SP	*B*	400.2	49.5	28.1 ± 14.6	-19.4 ± 14.5	34.1 ± 14.6	162.7 ± 14.2
2023MAY	2023-06-03 17:03:20	996	640	500SP	*B*	433.4	86.9	36.0 ± 6.7	60.4 ± 6.7	70.3 ± 6.7	29.6 ± 2.7
2017AUG	2017-08-11 13:53:51	1506	640	500SP	*B*	435.3	74.0	21.8 ± 8.9	81.0 ± 8.9	83.9 ± 8.9	37.5 ± 3.0
2018AUG	2018-08-21 14:16:31	973	640	500SP	*B*	438.2	54.9	25.1 ± 6.8	83.2 ± 6.8	86.9 ± 6.8	36.6 ± 2.2
2023MAY	2023-06-03 16:17:39	983	640	g'	*B*	460.2	89.2	19.3 ± 2.5	95.1 ± 2.6	97.0 ± 2.6	39.3 ± 0.8
2018MAR^s	2018-04-06 17:39:10	1032	640	g'	*B*	461.7	81.5	71.3 ± 2.5	99.9 ± 2.5	122.7 ± 2.6	27.2 ± 0.6
2018MAR^l	2018-04-06 17:19:21	1189	640	g'	*B*	461.8	81.6	16.2 ± 2.9	95.5 ± 2.7	96.9 ± 2.8	40.2 ± 0.8
2014AUG	2014-09-01 10:11:12	1843	640	g'	*B*	463.1	89.0	41.0 ± 3.6	164.0 ± 3.6	169.0 ± 3.6	38.0 ± 0.6
2017JUN	2017-06-26 16:02:50	1588	800	g'	*B*	463.3	86.8	13.4 ± 6.0	102.0 ± 4.2	102.9 ± 5.1	41.3 ± 1.7
2016FEB	2016-03-01 18:37:33	973	480	g'	*B*	463.8	86.9	27.6 ± 3.7	88.8 ± 3.7	93.0 ± 3.7	36.4 ± 1.2
2016FEB	2016-02-29 18:34:56	1012	480	g'	*B*	463.9	87.0	36.2 ± 4.0	85.1 ± 4.1	92.5 ± 4.0	33.5 ± 1.2
m2016JUL	2016-08-31 10:37:32	1609	800	Clear	*B*	464.0	74.3	43.5 ± 19.9	123.2 ± 20.6	130.7 ± 20.3	35.3 ± 4.4
m2016JUN	2016-06-10 10:47:32	1850	800	Clear	*B*	467.9	75.5	29.5 ± 21.9	98.45 ± 21.8	102.7 ± 21.8	36.7 ± 6.2
2018JUL	2018-07-25 16:08:13	1025	640	*V*	*B*	532.3	96.6	39.8 ± 4.1	217.1 ± 4.1	220.7 ± 4.1	39.8 ± 0.5
2018AUG	2018-08-21 14:36:42	1345	960	*V*	*B*	532.4	95.7	45.2 ± 3.1	178.5 ± 3.0	184.1 ± 3.1	37.9 ± 0.5
2023MAY	2023-06-03 17:23:21	1405	960	r'	*B*	601.8	64.2	31.5 ± 7.5	261.8 ± 6.7	263.7 ± 7.1	41.6 ± 0.8
2018JUL	2018-07-25 16:26:18	1045	710	r'	*B*	602.0	88.9	51.0 ± 7.3	262.8 ± 6.4	267.7 ± 6.8	39.5 ± 0.8
2017AUG	2017-08-09 13:12:24	1880	640	r'	*R*	619.2	80.7	61.1 ± 3.9	281.3 ± 3.7	287.9 ± 3.8	38.9 ± 0.4
2017AUG	2017-08-08 14:18:24	1339	640	r'	*R*	619.3	80.7	63.8 ± 3.7	283.9 ± 3.7	291.0 ± 3.7	38.7 ± 0.4
2016FEB	2016-02-27 16:41:49	1237	640	r'	*R*	619.9	80.6	30.3 ± 5.2	227.5 ± 5.4	229.5 ± 5.3	41.2 ± 0.7
2023MAY	2023-06-03 18:24:03	958	640	r'	*R*	620.8	60.5	64.5 ± 5.1	284.8 ± 5.2	292.0 ± 5.2	38.6 ± 0.5
2018MAR^l	2018-03-18 18:49:50	980	640	r'	*R*	620.9	84.5	78.4 ± 3.2	276.1 ± 3.2	287.0 ± 3.2	37.1 ± 0.3
2018MAR^s	2018-03-18 19:11:58	1300	640	r'	*R*	620.9	84.5	71.9 ± 4.6	278.7 ± 4.4	287.8 ± 4.4	37.8 ± 0.5
2017JUN	2017-07-04 13:08:09	2165	1440	650LP	*R*	717.6	62.7	81.9 ± 4.8	328.5 ± 4.8	338.6 ± 4.8	38.0 ± 0.4
2023MAY	2023-06-03 18:45:19	1634	1280	650LP	*R*	719.1	44.6	101.3 ± 8.1	341.2 ± 8.5	355.9 ± 8.3	36.7 ± 0.7
2018AUG	2018-08-23 11:47:56	1232	960	650LP	*R*	720.9	76.8	52.4 ± 4.1	318.2 ± 4.1	322.5 ± 4.1	40.3 ± 0.4

Notes. $^{s/l}$ Aperture sizes are as given in Table 1 except where indicated by these superscripts (*l*: 25.5″, *s*: 5.3″)—small enough to exclude the reported debris disk but not the binary companion (Rodriguez & Zuckerman 2012).
[a] *B* and *R* indicate blue- and red-sensitive H10720-210 and H10720-20 photomultiplier-tube detectors, respectively.

Table 3
Measurements of the ϵ Sgr Binary System

UT Date	ρ (arcsec)	pa (deg)	Δm (mag)	References
1992-06-18	2.06 ± 0.01	142 ± 1	5.85 (V)	(1)
1999-03[a]	2.39	142	4.6 (K)	(2)
2016-09-10	2.58 ± 0.04	140 ± 1	4.2 (2.3 μm)	(3)

Note.
[a] The exact date of the observation is not reported.
References. (1) Golimowski et al. (1993), (2) Hubrig et al. (2001), (3) This paper (Section 2.2).

expected to have significant intrinsic polarization (Cotton et al. 2017b).

2.3. Archival Spectroscopy

Spectra of ϵ Sgr have been obtained from the archive of the Canada–France–Hawaii Telescope (CFHT). These were taken with the Echelle Spectropolarimetric Device for Observation of Stars (ESPaDOnS) instrument (Donati 2003) on 2014 September 8. The spectra cover 370–1000 nm at $R \sim 70{,}000$. The individual integrations have been combined to form a single spectrum, which was used for the analysis in Sections 3.3 and 3.4.

We also used three spectra covering the Hα region taken with the Ultraviolet and Visual Echelle Spectrograph (UVES; Dekker et al. 2000) on the European Southern Observatory (ESO) Very Large Telescope (VLT).[7] These cover 472.6–683.5 nm and have $R = 74{,}450$. The dates of observation were 2016 April 22, May 17, and June 1.

3. Modeling

3.1. Polarization of Rotating Stars

We model the polarization of rotating stars using the methods described in detail by Bailey et al. (2020a) and also used by Cotton et al. (2017a), Lewis et al. (2022), and Howarth et al. (2023). We use a Roche model for the rotating star and assume gravity darkening according to Espinosa Lara & Rieutord (2011). This allows us to determine the distribution of local temperature and gravity as a function of latitude. We use a set of custom ATLAS9 (Castelli & Kurucz 2003) models to represent the local stellar atmosphere at 46 colatitudes from 0° to 90° at 2° steps. For each of these model atmospheres, we then calculate the specific intensity and polarization of the emergent radiation. These calculations use a version of the SYNSPEC spectral synthesis code (Hubeny et al. 1985; Hubeny 2012), which we have modified to do full polarized

[7] Based on data obtained from the ESO Science Archive Facility with doi:10.18727/archive/50.

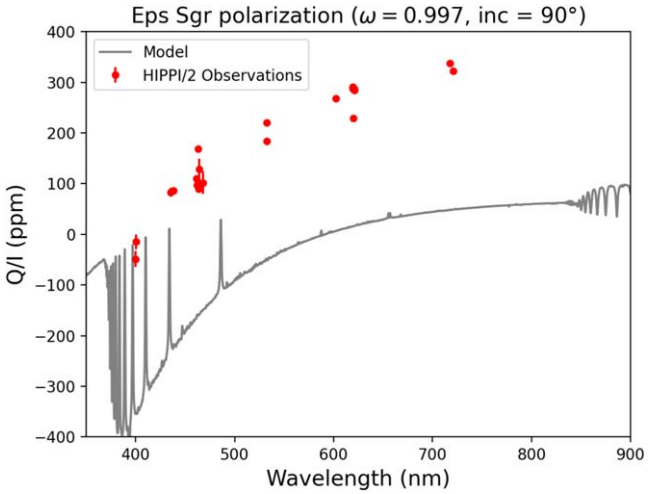

Figure 1. Polarization observations (rotated to put all the polarization into the Q Stokes parameter) compared with a model of polarization for a rapidly rotating star. The observations show similar wavelength dependence to the model but the polarization is offset by ∼300 ppm in the positive direction.

radiative transfer using the vector linearized discrete ordinate radiative transfer (VLIDORT) code of Spurr (2006).

We overlay a rectangular grid of pixels over the projected view of the star. For each pixel, we then determine the local temperature, gravity, and the surface-normal viewing angle. We then use these values to interpolate in our set of radiative transfer calculations to determine the local specific intensity and polarization. Summing over all the pixels then gives the integrated flux and polarization as a function of wavelength.

3.2. Polarization Components

Figure 1 shows the polarization observations rotated through ∼40°, which puts the polarization primarily in the Q Stokes parameter. The polarization shows a large change with wavelength from values of about −50 ppm at ∼400 nm to more than 300 ppm at ∼720 nm. This large wavelength change matches that expected for a star with a large rotation rate. However, when we compare the observations with a rapidly rotating-star model, as shown in Figure 1, we find that the observed polarization is offset in a positive direction from the modeled value by ∼300 ppm. In this plot negative polarization is perpendicular to the star's rotation axis, and positive polarization is parallel to the axis.

For the polarization to be consistent with rotational distortion, there must be an additional source of polarization of ∼300 ppm with a position angle parallel to the star's rotation axis. In our previous studies of rotating stars, we have been able to model the observations using a rotating-star model and a small contribution of interstellar polarization. For ϵ Sgr at a distance of 44 pc (van Leeuwen 2007), the expected level of interstellar polarization is ∼60 ppm according to the models of Cotton et al. (2017b) and a value as high as 300 ppm would be extremely unlikely (see Appendix). Furthermore, the interstellar polarization would have to be aligned with the rotation axis of the star to provide the required offset. This would not be consistent with what is measured for nearby stars and seems intrinsically unlikely.

For ϵ Sgr there is, however, an additional likely source of polarization with the required properties. The narrow shell absorption features in the spectrum, as described in Section 1, indicates the presence of circumstellar gas. In such a rapidly rotating star this is most likely in the form of a narrow equatorial disk. Such disks are common in rapidly rotating B stars, as seen in the classical Be stars (Rivinius et al. 2013). One of the important observable features of Be stars is polarization due to starlight scattered from the disk. The typical polarization level in nearby Be stars (where interstellar polarization is unimportant) is ∼3000–6000 ppm (Cotton et al. 2016a).

The much lower polarization (∼300 ppm) we infer for the disk in ϵ Sgr, as well as the lack of strong Hα emission, indicates a disk of much lower density than those usually found in classical Be stars. At low densities, we expect electron scattering to be the dominant opacity source leading to a flat, wavelength-independent polarization (Halonen & Jones 2013; Rivinius et al. 2013). This differs from the wavelength-dependent polarization structure seen in the higher-density disks of classical Be stars (Poeckert et al. 1979; Wood et al. 1997), where bound–free absorption is important. Comparison with the models of Halonen & Jones (2013) suggests a gas density of $\sim 10^{-13}$ g cm^{-3}, whereas densities up to $\sim 10^{-10}$ g cm^{-3} are seen in classical Be stars.

The polarization position angle of a Be star disk is perpendicular to the disk (Quirrenbach et al. 1997). Hence the polarization is parallel to the star's rotation axis, as required for our offsetting polarization component.

3.3. Polarization Variability

The polarization observations of ϵ Sgr (Table 2) show considerable scatter between observations in the same filter on different dates. The total range in p values is 77 ppm at g' and 62 ppm at r'. This is much larger than the statistical errors, and much larger than the scatter seen in our similar observations of other rapidly rotating stars using the same instruments (e.g., Bailey et al. 2020a; Howarth et al. 2023). The most extreme values are seen in some of the earliest observations in 2014 and 2016, whereas observations closely spaced in time generally show good agreement. This suggests variability of the polarization on long timescales. Such variability is not unexpected for a system with a disk component as described in the previous section. Polarization in Be stars is often variable (Coyne 1976).

Independent evidence for a variable Be-type disk in ϵ Sgr comes from the archival spectroscopy (Section 2.3). Figure 2 shows two spectra of ϵ Sgr. One of these, the CFHT spectrum from 2014 September 8, shows weak double-peaked emission in Hα. The other spectrum, taken on 2016 April 22 with VLT/UVES, shows a broad photospheric absorption and narrow shell absorption core. Similar behavior is seen in the other UVES spectra from 2016. Since the earlier spectroscopy discussed in Section 1 makes no mention of emission, we assume the 2016 spectra represent the more usual state. Interestingly, the highest g' polarization was observed on 2014 September 1, only a few days before the spectrum showing the emission, whereas polarization observations in 2016 show some of the lowest values.

3.4. Model Grid

The polarization of a rotating-star model (as described in Section 3.1) depends on four main parameters: the polar temperature and gravity (T_p, g_p), the rotation rate ($\omega = \Omega/\Omega_{\rm crit}$),

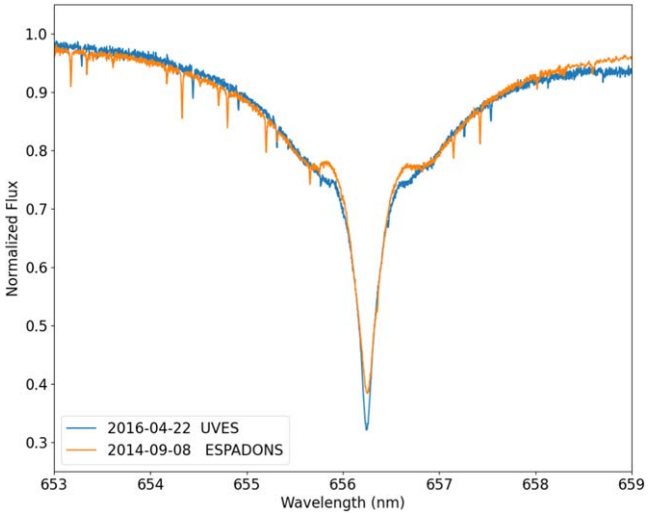

Figure 2. Spectra of ϵ Sgr in the Hα region. The UVES (ESO VLT) spectrum is from 2016 April 22 and shows broad absorption and the narrow shell absorption component. The ESPaDOnS (CFHT) spectrum on 2014 September 8 shows additionally double-peaked core emission. The very narrow absorption features are telluric lines.

and the inclination of the star's rotation axis (i).[8] The polarization observations alone are not sufficient to determine these four parameters so, as in our previous studies (Bailey et al. 2020a; Lewis et al. 2022; Howarth et al. 2023), we use additional information to provide relationships between these parameters.

The first of these is the spectral energy distribution (SED), which principally constrains the temperature and angular diameter (i.e., radius). We use photometry from Johnson et al. (1966; optical) and archival spectroscopy obtained with the International Ultraviolet Explorer (IUE; UV). IUE spectra taken in low-resolution mode ($\Delta\lambda \simeq 0.6$ nm) through the spectrographs' large aperture provide the most reliable spectrophotometry. Only one spectrum is available for each of the short- and long-wavelength ranges ($\lambda\lambda \simeq 115$–198, 185–335 nm), but the data are well exposed (SWP 16443, LWR 12689). We adjusted the fluxes to match the current Hubble Space Telescope calibration by using results from Massa & Fitzpatrick (2000), including the minor update described by Fitzpatrick et al. (2019). This gives an ∼8% increase in integrated UV flux over the standard pipeline product (and a ∼1.5% increase in the inferred $T_{\rm eff}$). The resulting integrated observed flux in the adopted 123.5–321 nm region is 1.40×10^{-6} erg cm^{-2} s^{-1}. We then applied an extinction correction for $E(B-V) = 0\overset{\rm m}{.}008$, estimated using the G-TOMO tool (based on results from Lallement et al. 2022), with a Seaton (1979) extinction curve (adopting $R \equiv A(V)/E(B-V) = 3.1$).[9]

The second constraint is the value of $v_{\rm e} \sin i$. We determined new values of $v_{\rm e} \sin i$ using a Fourier-transform analysis of archival CFHT spectra. We used the Mg II 448.1 nm line, chosen as the rotational line shape is less affected by shell absorption than alternatives such as Si II 634.7 nm. The analysis was done by comparing model spectra, calculated using Roche geometry, to the observations in Fourier-transform space (see Howarth et al. 2023, for a more detailed description of this approach). Because of the rotational distortion of the star and the strong gravity darkening, the inferred $v_{\rm e} \sin i$ values depend on the rotation rate ω, as shown in Figure 3. For slow rotations (alone) the inferred $v_{\rm e} \sin i$ is in reasonable agreement with the value of 236 km s^{-1} given by Royer et al. (2002).

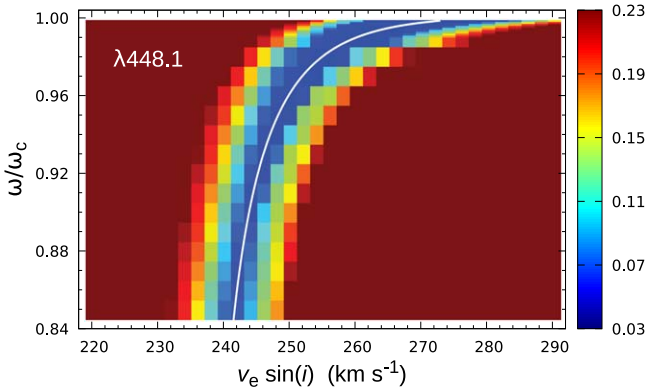

Figure 3. Results of Fourier-transform modeling of CFHT spectra of the Mg II 448.1 nm line to determine $v_{\rm e} \sin i$. The value plotted is the rms difference between observed and modeled Fourier transforms.

We adopt the $v_{\rm e} \sin i$–ω relation of Figure 3, together with the the Hipparcos parallax of 22.76 ± 0.24 mas (van Leeuwen 2007; the star is too bright for Gaia). We can then construct a two-dimensional grid of stellar parameters where all other values can be established from the two parameters ω and i. Each model in this grid corresponds to a star that fits the SED and $v_{\rm e} \sin i$. We can then calculate the polarization for each of these grid models and compare with the observations.

3.5. Comparison with Observations

In comparing the model grid calculations with the observations, we have to contend with the variability of the system (Section 3.3) and the presence of additional polarization components due to the disk and interstellar polarization (Section 3.2). There is insufficient data to attempt to correct for the variability. However, examination of the polarization measurements shows that the earliest observations (those in 2014 to 2016) seem to show the largest scatter, and variability at these times is confirmed by the spectra shown in Figure 2. We therefore chose to exclude these observations from the analysis, which was restricted to the 22 observations covering 2017–2023. There is still some evidence of variability, which shows up as excess noise compared with that expected from the measurement errors.

The additional polarization components were handled by fitting the observations with several variants of the model. The same grid of calculations was used for the polarization of the distorted star, but different models were used for the polarization of the additional components. Initial tests over a wider and coarser grid of models showed that only the models with high ω were compatible with the polarization. The final grid covered the range $0.980 \leqslant \omega \leqslant 0.999$ and $70 \leqslant i \leqslant 90$, and the relevant section of this region is shown in Figures 4–6.

In the first variant (Figure 4), we represent the additional polarization as a fixed (i.e., wavelength-independent) offset in Q and U. Thus at each point in the grid we fit three values, the Q offset, U offset, and the position angle of the star's rotation axis ($\theta_{\rm rot}$). With this model, we find that for the best-fitting (lowest-χ^2) points in Figure 4, the additional QU offset

[8] Where the subscript "crit" is used to denote critical rotation throughout this paper.

[9] https://explore-platform.eu/sdas

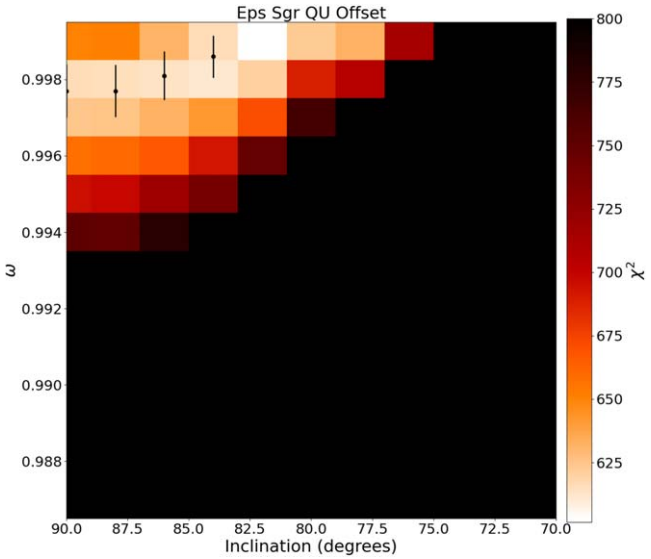

Figure 4. Fit to ϵ Sgr grid using the rotational polarization models plus a fixed polarization offset. In this and similar figures each point on the grid corresponds to a set of stellar parameters that fits the SED and $v_e \sin i$ of ϵ Sgr as described in Section 3.4. The plot shows how well each of these grid models fits the polarization observations.

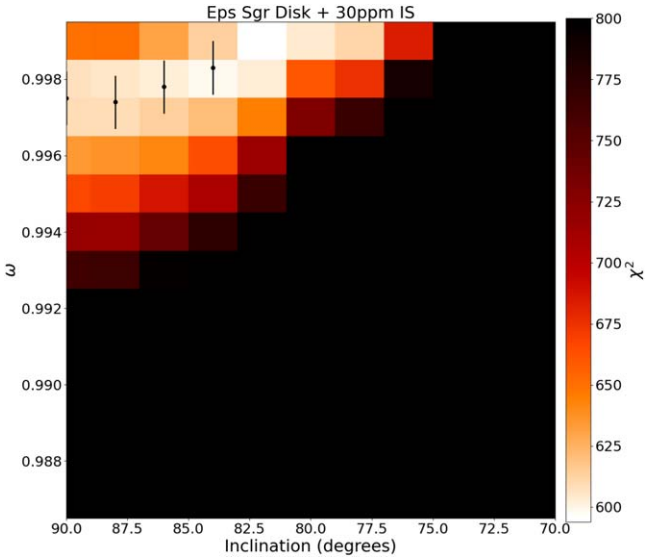

Figure 5. As Figure 4 but using the rotational polarization models plus a disk and up to 30 ppm interstellar component.

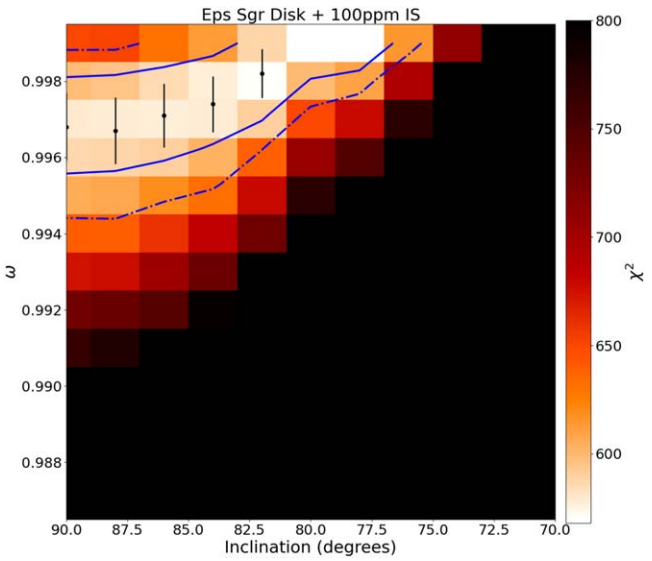

Figure 6. As Figure 4 but using the rotational polarization models plus a disk + up to 100 ppm interstellar component. The solid lines show the 2σ contours on the rotational parameters as fitted to these models (see Section 3.6). The dashed–dotted lines show the corresponding extended range of parameters when the uncertainties on the input parameters to the model grid (in particular $v_e \sin i$) are taken into account.

corresponds to a position angle of 38.5°, and the star's rotation axis is at 40.1°. The polarization is within 1.6° of that expected for an equatorial disk (Section 3.2). The small difference in angles can be understood as due to an additional contribution from interstellar polarization.

In the remaining variants, we represent the additional polarization as a combination of a wavelength-independent disk contribution and an interstellar-polarization component following the "Serkowski law" (Serkowski 1973; Serkowski et al. 1975; Wilking et al. 1982; Whittet et al. 1992). We set the λ_{max} of the interstellar polarization to 470 nm, the typical value found within the Local Hot Bubble (Marshall et al. 2020, and references within). In these models there are four fitted parameters at each grid point: p_{max} and the position angle θ_{ism} of the interstellar polarization, the position angle θ_{rot} of the star's rotation axis, and the polarization of the disk p_{disk}. The disk is assumed to be in the equatorial plane so its polarization position angle is θ_{rot}.

There is some degeneracy in these models between p_{max} and p_{disk}. We therefore ran three versions of the models where we applied the restricted ranges $0 < p_{max} \leqslant 30$ ppm, $0 < p_{max} \leqslant 60$ ppm, and $0 < p_{max} \leqslant 100$ ppm, based on our analysis of the likely value of interstellar polarization as described in the Appendix. Although we constrain p_{max} to a range, the best-fitting models in all these cases have p_{max} at the largest allowed value. The results for two of these cases are plotted in Figures 5 and 6, and all the variants are described in Table 4.

All these variants (Figures 4–6) produce quite similar results, with a "valley" of low-χ^2 values running from $\omega \sim 0.997$ at $i = 90°$ to $\omega = 0.999$ at $i \sim 80°$. Thus despite different assumptions about the interstellar polarization, almost the same stellar parameters are being selected in all these cases.

In Table 5, we list the stellar parameters corresponding to the two grid models at the ends of this χ^2 valley. The model labeled "Best" (in the "Disk + 100 ppm" set) is the one that has the lowest χ^2 and is at $\omega = 0.999$, $i = 80°$ (in some of the other model variants the best fit is in the adjacent grid point at $i = 82°$). However, the very strong shell absorption seen in ϵ Sgr, despite the low density of the disk, might favor a higher-inclination model like the $\omega = 0.997$, $i = 90°$ case also listed in Table 5.

Figure 7 shows images of the stellar models for the two cases listed in Table 5. The models show the distribution of specific intensity over the star, showing the strong effect of gravity darkening at the equator, and is overlaid with polarization vectors. The polarization is dominated by light from the bright regions at the top and bottom of the image, resulting in the negative (perpendicular to the rotation axis) integrated polarization at this wavelength.

Table 4
Parameters of Best-fit Region in Grid Model Variants (Figures 4–6)

Variant	*QU* Offset	Disk + Interstellar		
p_{max} (ppm)	0.0	30.0	60.0	100.0
θ_{ism} (deg)[a]	…	144.3	137.1	134.2
p_{disk} (ppm)[a]	276	299	330	367
θ_{rot} (deg)	40.1	39.9	39.9	39.9
$\omega(i = 90)$	0.9977(7)	0.9975(7)	0.9972(7)	0.9968(9)
$\omega(i = 88)$	0.9977(7)	0.9974(7)	0.9971(7)	0.9967(9)
$\omega(i = 86)$	0.9981(6)	0.9978(7)	0.9975(7)	0.9971(8)
$\omega(i = 84)$	0.9986(6)	0.9983(7)	0.9979(6)	0.9974(7)
$\omega(i = 82)$	0.999	0.999	0.9987(5)	0.9982(6)
$\omega(i = 80)$	…	…	0.999	0.999

Notes. Figures in parentheses are the errors in the last digit of the value. When the best fit for an inclination is in the $\omega = 0.999$ bin, the value given is the bin center and no error can be determined.
[a] Varies slightly with inclination; average value is given.

Table 5
Best-fitting Stellar Parameters

Parameter	$i = 90$[a]	Best[a]	Range[b] (2σ)
ω	0.997	0.999	0.995–1.0
v_e/v_{crit}	0.95	0.97	0.94–1.0
Inclination, i (deg)	90	80	76–90
T_{eff} (K)	10091	9950	9845–10096
T_p (K)	11791	11721	11548–11813
T_e (K)	7884	7433	7324–7492
$\mathrm{Log}(L/L_\odot)$	2.709	2.696	2.669–2.726
R_p ($R_\odot$)	5.98	6.01	5.90–6.08
R_e ($R_\odot$)	8.59	8.80	8.47–8.89
Mass ($M_\odot$)	3.69	3.80	3.69–3.90
$\log g_p$ (dex cgs)	3.45	3.46	3.45–3.48
$\log g_e$ (dex cgs)	2.24	2.00	1.99–2.36
P_{rot} (days)	1.63	1.61	1.57–1.64

Notes.
[a] The parameters listed are those of the grid model (see Section 3.4) giving the lowest χ^2 among all models ("Best"), and the best model at an inclination of 90°.
[b] "Range" is the full range of stellar parameters corresponding to the region enclosed by the dotted–dashed lines in Figure 6.

3.6. Uncertainties

To determine the uncertainties on the fitted values of ω and i, we use the bootstrap method (Press et al. 2007). For each of the model grid variants, we ran the modeling on 1000 trials using random selections of the 22 observations with replacement (so that each observations can be selected more than once). For each trial, we determined the best ω value at each inclination by fitting the χ^2 values with a cubic function. We then determined the standard deviation of these values over the 1000 trials. These results give the errors on ω listed in Table 4 and plotted as error bars on Figures 4–6. This method of error determination does not depend on the errors on the individual polarization measurements, but on the actual scatter on the data, which is largely due to the polarization variability of the star.

Using these bootstrap results, we can determine the $\Delta\chi^2$ ranges corresponding to 1 or 2σ, and thus determine the 2σ contours on ω and i, which are shown as the solid lines in Figure 6. We use Figure 6 (the "Disk + 100 ppm" variant) as this gives the lowest χ^2 values and has a somewhat broader distribution in ω, but largely overlays the best-fit regions covered by the other model variants.

Additional uncertainties are introduced by the uncertainties in the input parameters to the model grid (Section 3.4). These were assessed by running the modeling for auxiliary grids calculated for adjusted values of $v_e \sin i$, parallax, and UV flux in turn. The most significant effect is that due to an estimated 10 km s^{-1} uncertainty in $v_e \sin i$, which has the effect of moving the χ^2 valley up and down in ω. This leads to the wider 2σ contours shown by the dashed–dotted lines in Figure 6. Uncertainties in parallax and UV flux do not significantly change the fitted values of ω and i, but do have a small effect on the relationship to other stellar parameters. The wider contours (dashed–dotted lines) were then used to determine the allowed range of each stellar parameter, as listed in Table 5.

4. Discussion

4.1. There Is No Polarizing Debris Disk

Previously, HIPPI observations of ϵ Sgr were reported by Cotton et al. (2016b). They interpreted the observed polarization in the context of the system's reported IR excess (Rodriguez & Zuckerman 2012). Cotton et al. (2016b) present a model comprising two dust components (to reproduce the continuum IR excess) in addition to the stars. A cold dust belt (responsible for the bulk of the IR excess) was assumed to be circumbinary, with a warm dust belt orbiting one of the two stars. A residual polarization of 30 ppm remained after accounting for polarization induced by the interstellar medium. To reproduce this, a fractional polarization of around 50% of the total IR excess would be required. Such a value is much higher than those measured for dust grains in other debris disks, which peak at around 20%–30% (e.g., Krivova et al. 2000; Graham et al. 2007; Anche et al. 2023). Since the Cotton et al. (2016b) model was proposed, work by Vandeportal et al. (2019) has shown that warm (mid-IR) excesses represent substantially lower dust masses and contribute less to polarization compared to cool (far-IR) excesses with lower fractional luminosities but representing greater dust masses. This further reduces the plausibility of the proposed disk model.

The large beam size of IRAS and the low Galactic latitude of the system ($|b| < 10°$) also lead to the possibility that the flux density measurement at 60 μm is contaminated by diffuse background emission. Indeed, the IRAS point source catalog (Joint Iras Science 1994) notes a quality flag of "2" for the 60 μm band. Applying a downward revision of the flux, as implied, would only increase the tension between the level of IR excess and the polarization efficiency of the disk dust required.

In light of the observations presented here, we can eliminate the disk model as a plausible explanation for the polarimetric signal arising from the system. Specifically, the invariance of the position angle of the polarimetric signal between epochs, despite the secondary's proper motion, is inconsistent with illumination of a circumbinary dust disk. The agreement between the r' observations with small and large aperture sizes in the 2018MAR run is also inconsistent with this hypothesis. Furthermore, the level of fractional polarization required would be a factor of 2 higher than other systems for which such measurements are available (see above, and also Marshall et al. 2023).

Given that Rodriguez & Zuckerman (2012) find the system to be unstable with the accepted debris disk architecture and that IR excess may also be produced by free–free emission in

the (previously unidentified) Be disk (Kastner & Mazzali 1989), it is likely no debris disk exists at all. The nature of ϵ Sgr as a rapidly rotating B star with a gas disk is therefore the origin of its polarization.

4.2. Rapid Rotation

The rotation as a fraction of criticality that we measure for ϵ Sgr of $\omega \sim 0.997$, which corresponds to $v_e/v_{crit} \sim 0.95$, is the largest yet measured for a star in our Galaxy.[10] The previous highest was obtained by Domiciano de Souza et al. (2014), who measured the rotation of Achernar (HD 10144, hereafter α Eri) using interferometry as $\omega = 0.980$, $v_e/v_{crit} = 0.883$. α Eri is a Be star, but the measurements were made during a quiescent phase where the Be disk was absent.

ϵ Sgr stood out in our polarization study of bright, rapidly rotating stars because of the large amplitude of the wavelength-dependent polarization variations: >300 ppm, compared with <100 ppm for the other rapidly rotating stars (Cotton et al. 2017a; Bailey et al. 2020a; Howarth et al. 2023). Figure 8 shows how the observed polarization amplitude requires a large rotation rate, and cannot be matched with models for slower rotation. The only other star with a comparable polarization amplitude was θ Sco (Lewis et al. 2022). In that case, the rotation was slower than in ϵ Sgr, but the low gravity of this evolved star enhanced the polarization.

Multiwavelength polarimetry should therefore be a good way of finding other similar extreme rotators, and establishing how common such objects are. In the 19 stars we have observed for our AAT polarimetry program on rotating stars, we have found no other candidates for such extreme rotation. The program is based on stars down to $V \sim 3.5$ from the list of van Belle (2012).

4.3. Relationship to Be Stars

The value of $v_e/v_{crit} \sim 0.95$ that we find for ϵ Sgr is interesting because this is the value that was suggested (Townsend et al. 2004; Owocki 2005) as required for "weak" processes such as pulsation to be able to launch material from the star into orbit. If all Be stars rotated this fast, the existence of Be disks would be easier to explain. However, statistical analysis of $v_e \sin i$ data for Be stars (Cranmer 2005; but see Howarth 2007; Zorec et al. 2016) suggests that most Be stars rotate much slower than this, with a broad distribution of v_e/v_{crit} values from ~0.5 to ~0.95, with the mode of the distribution at 0.66 (Zorec et al. 2016). There are also rapidly rotating B stars (e.g., Regulus; Cotton et al. 2017a) that are not Be stars.

While ϵ Sgr has a rotation rate at the top end of the range inferred for Be stars, it is certainly not a typical classical Be star. It does appear to have an equatorial disk, but it is very weak compared with typical Be stars. Weak Hα emission has been observed on one occasion but is normally absent, as discussed in Section 3.3. Thus these results confirm that rotation alone cannot be the key requirement for formation of Be disks. Rather, there must be some additional mechanism operating in Be stars that can launch material from the surface into orbit. In ϵ Sgr this mechanism is either not operating or is operating with much reduced efficiency, enabling the formation of only a weak disk despite the very rapid rotation. We note

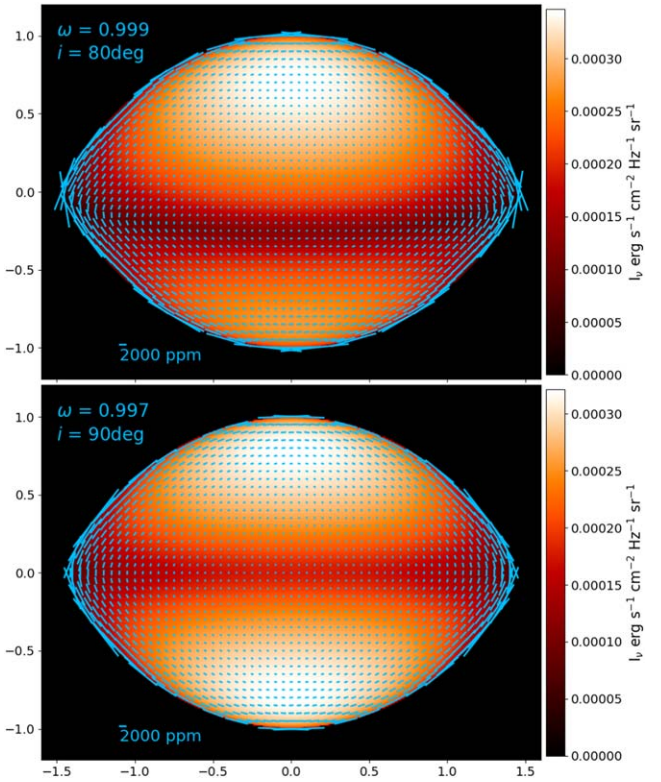

Figure 7. Polarization and intensity images for the two models of ϵ Sgr listed in Table 5. Specific intensity is overlaid with polarization vectors for a wavelength of 400 nm.

that classical Be stars are more common at early B spectral types and less common at the B9/A0 spectral type of ϵ Sgr. Huang et al. (2010) suggest that the threshold rotation rate for forming a Be disk is much higher for later-type stars.

Most classical Be stars show photometric variability on short timescales. Observations with the Transiting Exoplanet Survey Satellite (TESS; Ricker et al. 2015) typically show multiple periodic signals at frequencies between 0.5 and 4 day^{-1} (Labadie-Bartz et al. 2022). These are normally interpreted as nonradial pulsations, which may be related to the mass-ejection process that forms the disk (Rivinius et al. 2013).

In Figure 9, we show a periodogram of the TESS 2 minute cadence light curve of ϵ Sgr for Sector 13 (2019 June 19–July 17).[11] The pattern seen of two groups of peaks (here at ~0.65 and 1.3 day^{-1}), with a frequency ratio of roughly 1–2 is one that is very commonly seen in Be stars (e.g., Walker et al. 2005; Baade et al. 2018; Semaan et al. 2018; Labadie-Bartz et al. 2022). However, the amplitude (around 140 ppm for the highest peak) is low compared with those more typically seen in classical Be stars, which are in the parts per thousands (Labadie-Bartz et al. 2022).

As an example, we show in the lower panel of Figure 9 the periodogram of ϵ Sgr compared with that of the bright Be star α Eri, based on observations obtained from TESS Sector 2 (2018 August 23–September 20). At that time α Eri was in an active state. It has been quiescent without a disk since late 2019.[12] The frequency structure seen in α Eri is quite similar to that of ϵ Sgr, but the peak amplitude is 25 times higher in α Eri.

[10] VFTS285, an O star in the Large Magellanic Cloud, has been reported as having $\omega = 1.00$ (Shepard et al. 2022).

[11] The TESS data used here are available at MAST: doi:10.17909/t1ae-rd45.

[12] According to our polarization monitoring of α Eri over the last 10 yr.

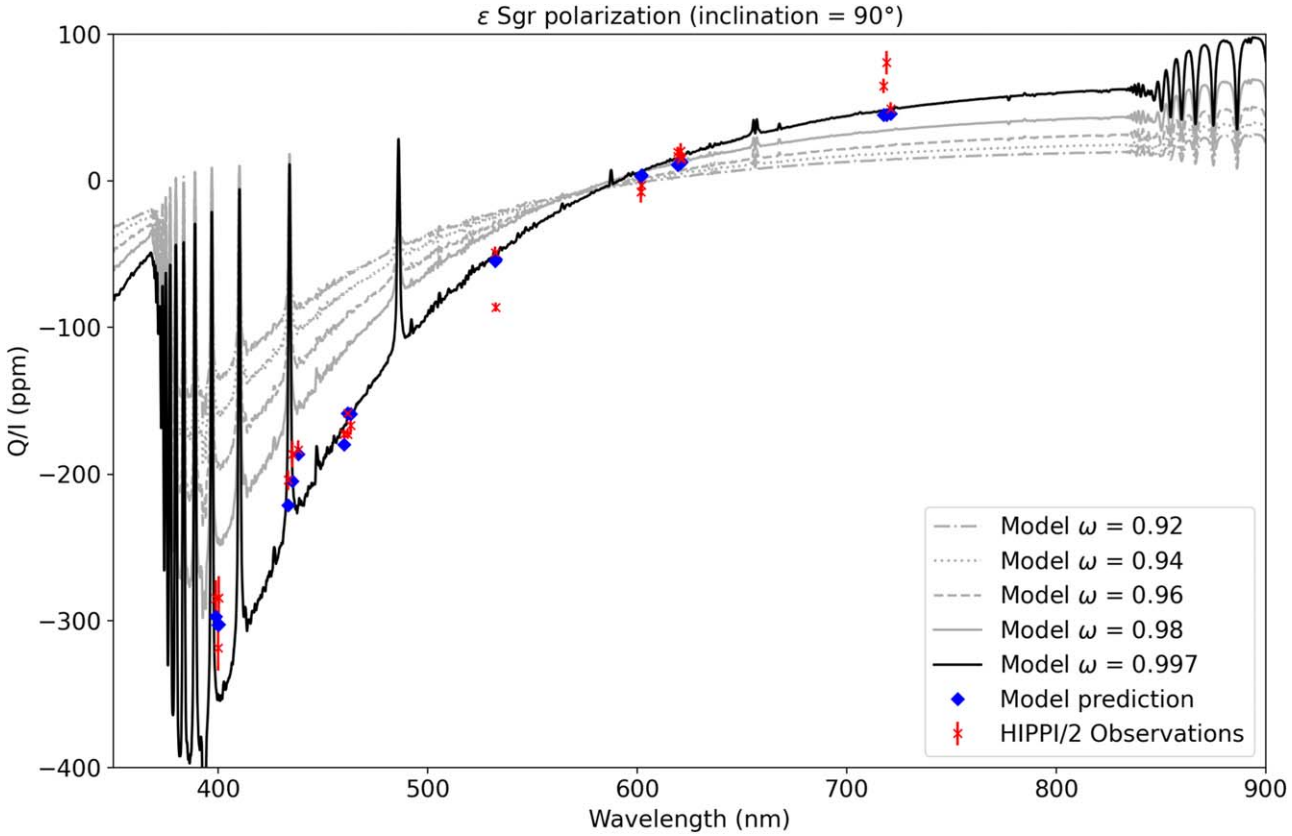

Figure 8. Comparison of observations and models for the polarization of ϵ Sgr as a function of wavelength. The models show the predictions due to stellar rotation. The disk and interstellar polarization have been applied as a correction to the observations. The black solid line is the model for $\omega = 0.997$, $i = 90°$. Blue diamonds are the predicted polarization values for each observed filter (they are not necessarily exactly on the line, because they are averages over the filter bandpass). Gray lines show the model predictions for grid models with lower values of ω.

4.4. Evolutionary Status

In Figure 10, we show the position of ϵ Sgr on the Hertzsprung–Russell (HR) diagram compared with evolutionary models for rotating stars of solar metallicity ($Z = 0.014$) from Georgy et al. (2013). The models are for $M/M_{\odot}$ of 3.0 and 4.0 (our measured value is $M/M_{\odot} = 3.69$), and initial rotation rates of $\omega = 0.7$, 0.8, and 0.9. The location of ϵ Sgr is that of a star just beginning to evolve away from the main sequence. Its position corresponds to the hydrogen-shell-burning phase where the star is crossing the Hertzprung gap. This is a very rapid phase of stellar evolution, and such stars are not commonly observed.

Figure 11 shows a comparison with the same set of models in a plot of ω against $\log(g_p)$. The $\log(g_p)$ we measure for ϵ Sgr is again consistent with a star beginning to evolve away from the main sequence. The maximum rotation rate for these model stars corresponds to the "hook" in the HR diagram where the star contracts after the end of core hydrogen burning. At this point a star born with $\omega = 0.9$ or greater reaches near-critical rotation. However, Figures 10 and 11 show that our measured parameters for ϵ Sgr place the star at a point beyond the "hook" where the star is expanding and the rotation rate is slowing. The rotation we measure for ϵ Sgr is therefore too high to match any of these single-rotating-star models. Its rapid rotation may therefore be the result of close binary evolution (Pols et al. 1991).

The visible companion (Section 2.2) seems to have colors consistent with a main-sequence star, making it unlikely to have been involved in the interaction that caused the rapid rotation. ϵ Sgr is known to be an X-ray source (Berghoefer et al. 1996; Hubrig et al. 2001), which might indicate an unseen companion.

5. Future Observations

Our results on ϵ Sgr could be further tested by a number of other observations.

5.1. Interferometry

Interferometry has been successful in imaging the rotational distortion of a number of stars of similar brightness and spectral type to ϵ Sgr such as Regulus (Che et al. 2011), Altair (Monnier et al. 2007) and α Oph (Zhao et al. 2009). Such observations should be able to confirm the extreme rotational oblateness and detect the variation of surface brightness due to gravity darkening. Interferometry is better than polarimetry at measuring the inclination and hence distinguishing between the range of models that are consistent with the polarimetry.

5.2. Spectropolarimetry and the Öhman Effect

Current observations of the polarization due to the rotational distortion of stars, such as those presented in this paper, have been made with broadband polarimeters because these instruments can achieve the high precision needed to measure the small rotational signals. However, further information on stellar rotation could be obtained from spectropolarimetric observations with sufficient resolution to resolve the lines.

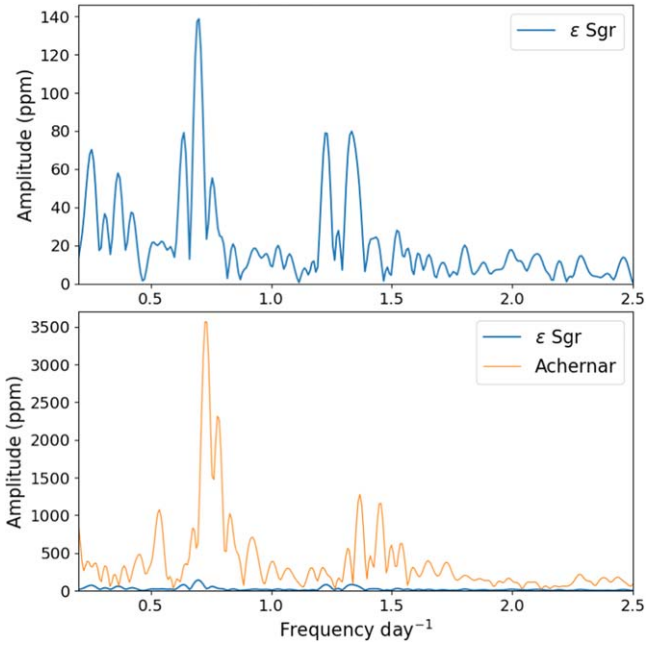

Figure 9. Periodogram of TESS light curve of ϵ Sgr (TESS Sector 13). In the upper panel it is shown at full scale. In the lower panel it is compared with a periodogram of the bright classical Be star Achernar (α Eri) from TESS Sector 2. The presence of two frequency groups with a 2:1 frequency ratio is common in Be stars, but the amplitude seen in ϵ Sgr is much lower than is commonly seen.

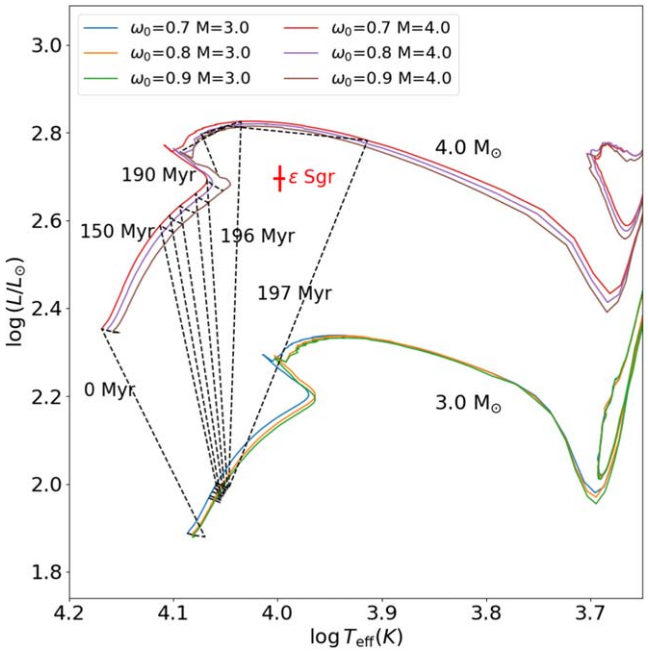

Figure 10. Location of ϵ Sgr on the HR diagram compared with evolutionary models for rotating stars from Georgy et al. (2013). Isochrones are shown at 10 Myr intervals from 150 to 190 Myr, and then at 196 and 197 Myr.

These effects include the Öhman effect first predicted in 1946 (Öhman 1946). The Öhman effect arises because at different points in the line profile of a rotationally broadened line the absorption arises in different parts of the star and therefore changes the integrated polarization we observe. Models of the effect have been given by Collins & Cranmer (1991). The effect is small and has not yet been observed. Since ϵ Sgr has the largest rotational signal yet seen in continuum

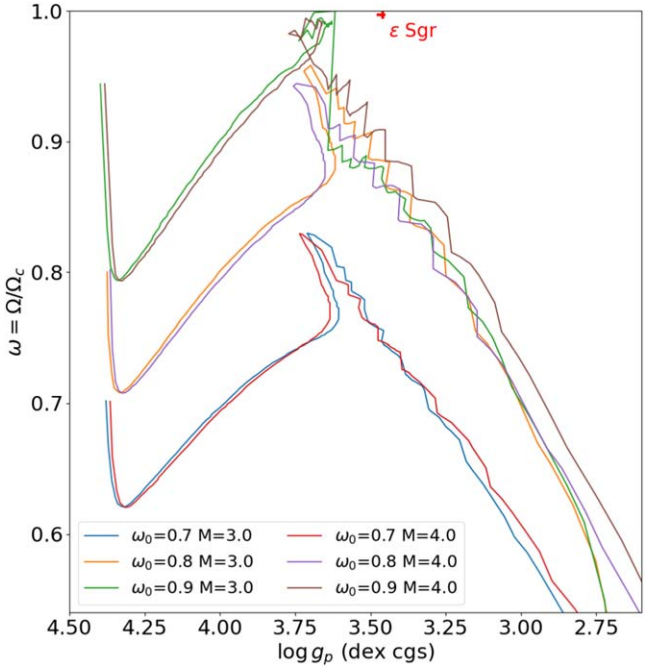

Figure 11. Plot of ω against $\log(g_p)$ for ϵ Sgr and the same models as in Figure 10. The rotation rate (ω) reaches a maximum at a point corresponding to the "hook" in the HR diagram, and then declines rapidly as the star evolves across the Hertzprung gap.

polarization, it is interesting to consider whether observations of the Öhman effect for this star are feasible and useful.

Because our polarization modeling using SYNSPEC/VLIDORT (Section 3.1) is carried out at high spectral resolution, our models predict what should be seen in spectropolarimetry. As in the modeling done by Collins & Cranmer (1991), the spectral lines are treated as pure absorbers. No line polarization processes are involved. The polarization is due to the same processes that produce the continuum polarization (primarily electron scattering).

Models for the polarization wavelength dependence of ϵ Sgr are shown in Figure 12 for the 380–450 nm region. This shows the problem with detecting the Öhman effect in a star of this spectral type. The spectrum is dominated by hydrogen lines, which are strongly Stark broadened by an amount that exceeds the rotational broadening. The pure Öhman effect is only seen on the metal lines, of which the Ca II K line at 393 nm is the strongest in this region. The large polarization features seen on the hydrogen lines in Q/I are not due to the Öhman effect, but are due to the fact that in these strong lines we are seeing different layers of the star in line and continuum.

The Öhman effect features seen in U/I are more interesting because they show a strong dependence on inclination. The features seen on the hydrogen lines are smeared out by the Stark broadening, but may still be observable and would provide another way of refining the inclination of the star. Such an observation would require spectropolarimetry with $R > 5000$ and precision $\sim$5 ppm or better.

5.3. Ultraviolet Polarimetry

Models of rotating stars predict that polarization values are expected to increase at shorter wavelengths (Collins et al. 1991; Jones et al. 2022), reaching $\sim$1% (10,000 ppm) at 120 nm for large ω and high inclination. Since the polarization due to a

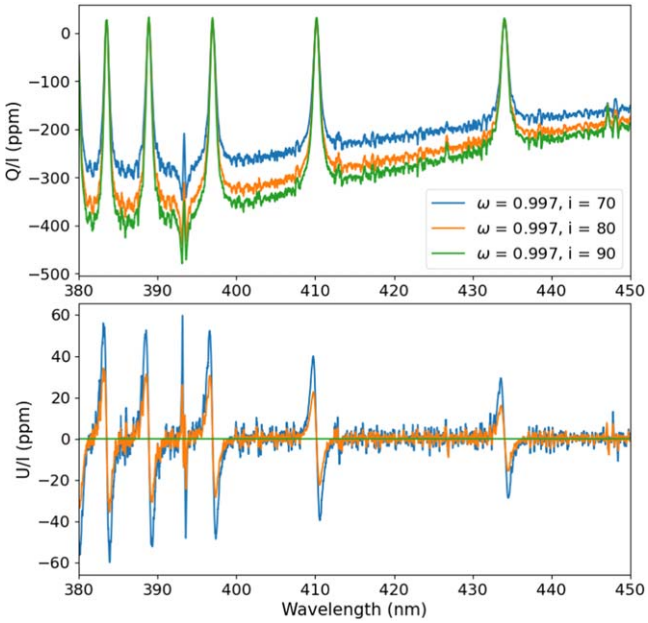

Figure 12. Modeled polarization for ϵ Sgr at high spectral resolution. The pure Öhman effect (due to rotational line broadening) is seen most clearly on the Ca II K line at 393 nm, the strongest metal line in this region. On the strongly Stark-broadened hydrogen lines (the five strongest lines in this region) the Öhman effect in Q/I is swamped by other effects, but the Öhman effect is still present in U/I, and is a strong function of inclination

disk is not strongly wavelength dependent, and interstellar polarization decreases at shorter wavelengths, observations in the UV would remove any possible confusion between these different sources. Such observations may be possible with future space missions similar to the proposed Polstar satellite (Scowen et al. 2022).

6. Conclusions

Multiwavelength, high-precision polarization observations of ϵ Sgr show the distinctive wavelength dependence expected for a rotationally distorted star, but with a much higher amplitude (∼300 ppm) than seen in other rapidly rotating stars. In order to fit a rotating-star model, an additional positive polarization component is needed. We attribute this to polarization in a low-density ($\sim 10^{-13}$ g cm^{-3}) equatorial gas disk which also produces the narrow shell absorption features seen in the spectrum.

Detailed modeling of the polarization together with additional data including the SED and $v_e \sin i$ reveals a very high rotation rate of $\omega \geqslant 0.995$, the highest yet measured for a star in our Galaxy. The modeling also results in a detailed set of stellar parameters. The star is rotating too rapidly to be consistent with single-rotating-star evolutionary tracks, suggesting that it is likely to be a product of binary evolution.

ϵ Sgr shares some features with Be stars in having a low-density gas disk, weak Hα emission seen on one occasion, and multiple periodicities in its TESS light curve. However, the disk is of very low density and the TESS periodicities are of very low amplitude compared with typical Be stars. The results confirm that rapid rotation alone cannot be the cause of the Be phenomenon, and support the idea that an additional mechanism is needed to eject material into a Be disk.

ϵ Sgr is an excellent target for future observations by interferometry, spectropolarimetry, and UV polarimetry, which would allow the extreme rotation to be confirmed and the stellar parameters refined.

Acknowledgments

Based in part on data obtained at Siding Spring Observatory. We acknowledge the traditional owners of the land on which the AAT stands, the Gamilaraay people, and pay our respects to elders past and present. J.P.M. acknowledges research support by the National Science and Technology Council of Taiwan under grant No. NSTC 112-2112-M-001-032-MY3. D.V.C. thanks the Friends of MIRA for their support.

Facilities: AAT (HIPPI, HIPPI-2, IRIS2), CFHT (ESPaDOnS), VLT:Kueyen (UVES), IUE, TESS.

Appendix
Interstellar Polarization

In Figure 13, we present a map of the polarization of nearby stars. The stars have been selected such that their polarization is likely to be interstellar dominated. We interrogated observations made with high-precision polarimeters, reported in Bailey et al. (2010, 2017, 2020a), Cotton et al. (2016a, 2017a, 2017b, 2019, 2020), Marshall et al. (2016, 2020, 2023), Bott et al. (2018), Piirola et al. (2020), and Lewis et al. (2022), and selected stars with spectral types between A0 and K2.5 within 35°. From this list we removed rapidly rotating stars, those in close binary systems, magnetically active stars, systems hosting significant debris disks, and any other star known to display intrinsic polarization. To this we added a small number of interstellar controls newly observed for this work (Table 6). The observations were not all made in the same bandpass so, as we have done in past work, we assumed $\lambda_{max} = 470$ nm and used the Serkowski law to scale the polarization magnitude to correspond to 450 nm—representative of the g' band.

The right panel of Figure 13 illustrates that most stars near ϵ Sgr have polarizations corresponding to $\leqslant 2$ ppm pc^{-1}, though the closest star, HD 169586, is a little greater. This is in line with the trends previously reported in Cotton et al. (2017b), which if extrapolated predict 60.0 ± 10.5 ppm for ϵ Sgr (gray dot).

The position angles of the interstellar controls are shown in the left panel of Figure 13. Cotton et al. (2017b) presents a formula for predicting the position angle of interstellar polarization for a star based on the angular separation weighted mean of nearby stars that gives $163.1° \pm 29.1$ (gray bar). However, this was only meant to apply to stars within 30 pc of the Sun, where potential controls are sparse. The paper also found better agreement than the nominal error between stars within 10° of each other on the sky; the median position angle of the nearest five stars to ϵ Sgr is 145.6°; it is likely that the interstellar position angle is within 15°–20° of this.

Table 6
Observations of Interstellar Control Stars

Control HD	SpT	Run	UT	Dwell (s)	Exp. (s)	$\lambda_{\rm eff}$ (nm)	Eff. (%)	q (ppm)	u (ppm)	p (ppm)	θ (deg)
157919	F5III-IV	2018MAR	2018-03-27 19:22:38	1114	640	468.3	84.2	18.5 ± 5.8	-20.4 ± 5.6	27.5 ± 5.7	156.1 ± 6.0
160691	G3IV-V	2018MAR	2018-04-04 17:15:17	1780	1280	472.1	85.7	14.5 ± 6.0	8.1 ± 5.9	16.6 ± 5.9	14.6 ± 11.2
165189	A6V	2018AUG	2018-09-01 10:51:27	971	640	464.4	58.7	-56.6 ± 11.7	0.1 ± 11.2	56.6 ± 11.5	89.9 ± 5.9
168723	K0III-IV	2018MAR	2018-03-29 19:00:51	1001	640	475.0	86.9	10.2 ± 4.6	22.7 ± 4.4	24.9 ± 4.5	32.9 ± 5.2
		2018JUL	2018-07-12 10:54:07	1100	640	475.3	86.1	1.7 ± 4.6	17.0 ± 4.5	17.1 ± 4.6	42.1 ± 7.8
177474	F8V	2017AUG	2017-08-14 13:49:16	1663	960	471.3	89.2	3.4 ± 5.8	-17.6 ± 5.9	17.9 ± 5.8	140.5 ± 9.9
181240	A8III	2018MAR	2018-04-05 18:40:37	1716	1280	465.3	83.0	-88.4 ± 6.9	-47.5 ± 6.9	100.4 ± 6.9	104.1 ± 2.0
		2018MAR	2018-04-06 18:25:17	1726	1280	465.4	83.0	-104.2 ± 6.7	-54.2 ± 6.6	117.5 ± 6.7	103.7 ± 1.6
191408	K2.5V	2016JUN	2016-06-25 12:21:58	3029	1680	477.2	90.9	-8.6 ± 9.3	-32.0 ± 8.7	33.1 ± 9.0	127.5 ± 8.0
192310	K2 + V	2016JUN	2016-06-25 15:41:28	3464	2560	476.1	90.7	-9.8 ± 7.2	-5.9 ± 7.1	11.4 ± 7.2	105.5 ± 22.3
		2018JUL	2018-07-20 13:21:57	2203	1600	475.3	86.0	-17.7 ± 6.9	-3.5 ± 8.3	18.0 ± 7.6	95.6 ± 13.9
[R]		2018JUL	2018-07-23 11:07:49	1772	1280	627.0	84.4	-14.8 ± 8.9	-18.4 ± 9.8	23.6 ± 9.3	115.6 ± 12.7
[R]		2018JUL	2018-07-23 11:33:17	1051	640	627.0	84.4	14.0 ± 12.0	-16.7 ± 12.3	21.8 ± 12.1	155.0 ± 19.7
192947	G9III	2018JUL	2018-07-18 12:25:25	1068	640	474.7	85.8	-16.1 ± 4.7	15.7 ± 4.7	22.5 ± 4.7	67.9 ± 6.1

Notes. The same aperture as used for the ϵ Sgr observations specified in Table 1 in the same run was used. Spectral types (SpT) are from SIMBAD.
[R] Indicates SDSS r' filter paired with R photomultiplier-tube detectors; all other tabulated observations used the SDSS g' filter paired with the B photomultiplier-tube detectors.

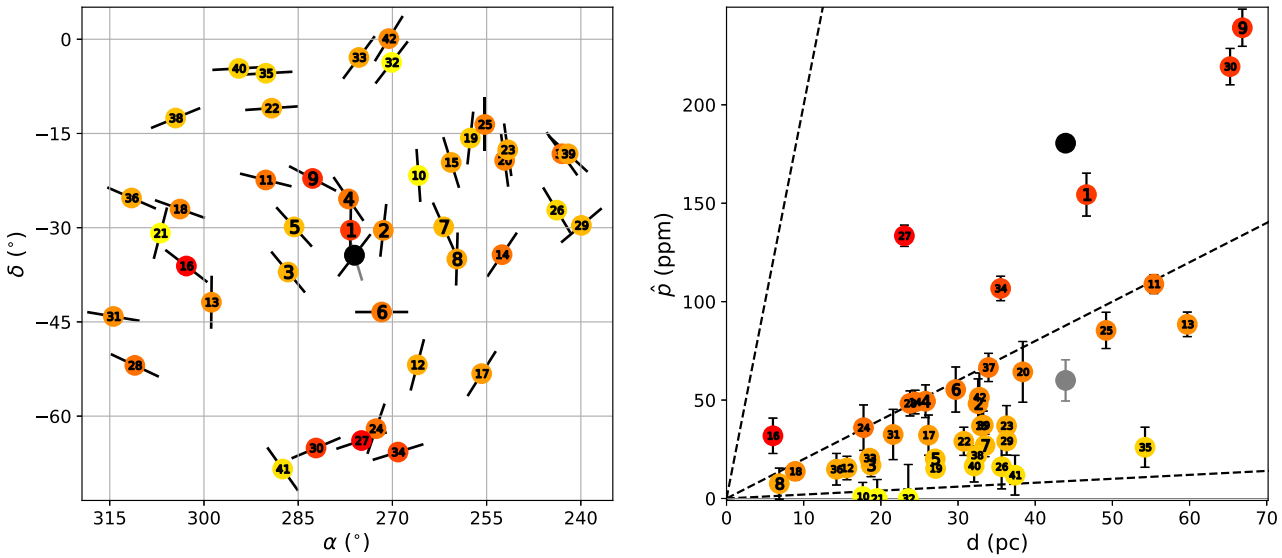

Figure 13. Plot of the polarization of stars near to ϵ Sgr, representative of interstellar polarization, as projected onto the sky (left)—vectors represent the position angle (PA, clockwise N over E)—and debiased according to $\hat{p} = \sqrt{p^2 - p_e^2}$ as a function of distance (right). Where multiple observations exist, the error-weighted average is displayed. The gray vector and dot represent the interstellar polarization of ϵ Sgr as predicted by the model in Cotton et al. (2017b), whereas their black counterparts average the observations and correct them for wavelength as if they are interstellar measurements. All observations are scaled to 450 nm as if they are purely interstellar with $\lambda_{max} = 470$ nm. The controls are numbered in order of angular separation as follows: 1: HD 169586, 2: HD 165135, 3: HD 177474, 4: HD 166916, 5: HD 176687, 6: HD 165189, 7: HD 157919, 8 HD 156384, 9: HD 174309, 10: HD 160915, 11: HD 181240, 12: HD 160691, 13: HD 188114, 14: HD 151680, 15: HD 157172, 16: HD 191408, 17: HD 153580, 18: HD 192310, 19: HD 155125, 20: HD 151504, 21: HD 194640, 22: HD 180409, 23: HD 151192, 24: HD 165499, 25: HD 153631, 26: HD 146070, 27: HD 167425, 28: HD 197157, 29: HD 143114, 30: HD 173168, 31: HD 199288, 32: HD 164259, 33: HD 168723, 34: HD 162521, 35: HD 181391, 36: HD 197692, 37: HD 145518, 38: HD 192947, 39: HD 144766, 40: HD 185124, 41: HD 177389, 42: HD 164651. Note that for stars with $p < \sigma_p$ the PAs in the left-hand panels are not well defined, since $\sigma_{PA} > 28°$.

ORCID iDs

Jeremy Bailey https://orcid.org/0000-0002-5726-7000
Ian D. Howarth https://orcid.org/0000-0003-3476-8985
Daniel V. Cotton https://orcid.org/0000-0003-0340-7773
Jonathan P. Marshall https://orcid.org/0000-0001-6208-1801
Lucyna Kedziora-Chudczer https://orcid.org/0000-0001-7212-0835

References

Anche, R. M., Douglas, E., Milani, K., et al. 2023, PASP, 135, 125001
Baade, D., Pigulski, A., Rivinius, T., et al. 2018, A&A, 610, A70
Bailey, J., Cotton, D. V., Howarth, I. D., Lewis, F., & Kedziora-Chudczer, L. 2020a, MNRAS, 494, 2254
Bailey, J., Cotton, D. V., & Kedziora-Chudczer, L. 2017, MNRAS, 465, 1601
Bailey, J., Cotton, D. V., Kedziora-Chudczer, L., De Horta, A., & Maybour, D. 2020b, PASA, 37, e004
Bailey, J., Kedziora-Chudczer, L., Cotton, D. V., et al. 2015, MNRAS, 449, 3064
Bailey, J., Lucas, P. W., & Hough, J. H. 2010, MNRAS, 405, 2570
Baschek, B., & Slettebak, A. 1988, A&A, 207, 112
Berghoefer, T. W., Schmitt, J. H. M. M., & Cassinelli, J. P. 1996, A&AS, 118, 481
Bott, K., Bailey, J., Cotton, D. V., et al. 2018, AJ, 156, 293
Bradley, L., Sipőcz, B., Robitaille, T., et al. 2022, astropy/photutils: v1.5.0, Zenodo, doi:10.5281/zenodo.6825092
Castelli, F., & Kurucz, R. L. 2003, in IAU Symp. 210, Modelling of Stellar Atmospheres, ed. N. Piskunov, W. W. Weiss, & D. F. Gray (San Fransisco, CA: ASP), A20
Che, X., Monnier, J. D., Zhao, M., et al. 2011, ApJ, 732, 68
Chen, C. H., Mittal, T., Kuchner, M., et al. 2014, ApJS, 211, 25
Collins, G. W., & Cranmer, S. R. 1991, MNRAS, 253, 167
Collins, G. W., Truax, R. J., & Cranmer, S. R. 1991, ApJS, 77, 541
Cote, J. 1987, A&A, 181, 77
Cotton, D. V., Bailey, J., Howarth, I. D., et al. 2017a, NatAs, 1, 690
Cotton, D. V., Bailey, J., Kedziora-Chudczer, L., et al. 2016a, MNRAS, 455, 1607
Cotton, D. V., Bailey, J., Pringle, J. E., et al. 2020, MNRAS, 494, 4591
Cotton, D. V., Marshall, J. P., Bailey, J., et al. 2017b, MNRAS, 467, 873
Cotton, D. V., Marshall, J. P., Bott, K., Kedziora-Chudczer, L., & Bailey, J. 2016b, arXiv:1605.07742
Cotton, D. V., Marshall, J. P., Frisch, P. C., et al. 2019, MNRAS, 483, 3636
Coyne, G. V. 1976, in IAU Symp. 70, Be and Shell Stars, ed. A. Slettebak (Dordrecht: Reidel), 233
Cranmer, S. R. 2005, ApJ, 634, 585
Dekker, H., D'Odorico, S., Kaufer, A., Delabre, B., & Kotzlowski, H. 2000, Proc. SPIE, 4008, 534
Domiciano de Souza, A., Kervella, P., Moser Faes, D., et al. 2014, A&A, 569, A10
Donati, J. F. 2003, in ASP Conf. Ser. 307, Solar Polarization, ed. J. Trujillo-Bueno & J. Sanchez Almeida (San Francisco, CA: ASP), 41
Espinosa Lara, F., & Rieutord, M. 2011, A&A, 533, A43
Fitzpatrick, E. L., Massa, D., Gordon, K. D., Bohlin, R., & Clayton, G. C. 2019, ApJ, 886, 108
Georgy, C., Ekström, S., Granada, A., et al. 2013, A&A, 553, A24
Golimowski, D. A., Durrance, S. T., & Clampin, M. 1993, AJ, 105, 1108
Graham, J. R., Kalas, P. G., & Matthews, B. C. 2007, ApJ, 654, 595
Gray, R. O., & Garrison, R. F. 1987, ApJS, 65, 581
Halonen, R. J., & Jones, C. E. 2013, ApJ, 765, 17
Harrington, J. P., & Collins, G. W. 1968, ApJ, 151, 1051
Houk, N. 1982, Michigan Catalogue of Two-dimensional Spectral Types for the HD Stars, Vol. 3 (Ann Arbor, MI: Univ. Michigan Press)
Howarth, I. D. 2007, in ASP Conf. Ser. 361, Active OB-Stars: Laboratories for Stellare and Circumstellar Physics, ed. A. T. Okazaki, S. P. Owocki, & S. Stefl (San Francisco, CA: ASP), 15
Howarth, I. D., Bailey, J., Cotton, D. V., & Kedziora-Chudczer, L. 2023, MNRAS, 520, 1193
Huang, W., Gies, D. R., & McSwain, M. V. 2010, ApJ, 722, 605
Hubeny, I. 2012, in IAU Symp. 282, From Interacting Binaries to Exoplanets: Essential Modeling Tools, ed. M. T. Richards & I. Hubeny (Cambridge: Cambridge Univ. Press), 221
Hubeny, I., Stefl, S., & Harmanec, P. 1985, BAICz, 36, 214
Hubrig, S., Le Mignant, D., North, P., & Krautter, J. 2001, A&A, 372, 152
Johnson, H. L., Mitchell, R. I., Iriarte, B., & Wisniewski, W. Z. 1966, CoLPL, 4, 99
Joint Iras Science, W. G. 1994, yCat, 2125, 0
Jones, C. E., Labadie-Bartz, J., Cotton, D. V., et al. 2022, Ap&SS, 367, 124
Kastner, J. H., & Mazzali, P. A. 1989, A&A, 210, 295

Krivova, N. A., Krivov, A. V., & Mann, I. 2000, ApJ, 539, 424
Labadie-Bartz, J., Carciofi, A. C., Henrique de Amorim, T., et al. 2022, AJ, 163, 226
Lallement, R., Vergely, J. L., Babusiaux, C., & Cox, N. L. J. 2022, A&A, 661, A147
Lewis, F., Bailey, J., Cotton, D. V., et al. 2022, MNRAS, 513, 1129
Marshall, J. P., Cotton, D. V., Bott, K., et al. 2016, ApJ, 825, 124
Marshall, J. P., Cotton, D. V., Bott, K., et al. 2023, MNRAS, 522, 2777
Marshall, J. P., Cotton, D. V., Scicluna, P., et al. 2020, MNRAS, 499, 5915
Massa, D., & Fitzpatrick, E. L. 2000, ApJS, 126, 517
Monnier, J. D., Zhao, M., Pedretti, E., et al. 2007, Sci, 317, 342
Öhman, Y. 1946, ApJ, 104, 460
Owocki, S. 2005, in ASP Conf. Ser. 337, The Nature and Evolution of Disks Around Hot Stars, ed. R. Ignace & K. G. Gayley (San Francisco, CA: ASP), 101
Paunzen, E., Duffee, B., Heiter, U., Kuschnig, R., & Weiss, W. W. 2001, A&A, 373, 625
Piirola, V., Berdyugin, A., Frisch, P. C., et al. 2020, A&A, 635, A46
Poeckert, R., Bastien, P., & Landstreet, J. D. 1979, AJ, 84, 812
Pols, O. R., Cote, J., Waters, L. B. F. M., & Heise, J. 1991, A&A, 241, 419
Press, W. H., Teukolsky, S. A., Vetterling, W. T., & Flannery, B. P. 2007, Numerical Recipes 3rd Edition: The Art of Scientific Computing (3rd ed.; Cambridge: Cambridge Univ. Press)
Quirrenbach, A., Bjorkman, K. S., Bjorkman, J. E., et al. 1997, ApJ, 479, 477
Rhee, J. H., Song, I., Zuckerman, B., & McElwain, M. 2007, ApJ, 660, 1556
Ricker, G. R., Winn, J. N., Vanderspek, R., et al. 2015, JATIS, 1, 014003
Rivinius, T., Carciofi, A. C., & Martayan, C. 2013, A&ARv, 21, 69
Rodriguez, D. R., & Zuckerman, B. 2012, ApJ, 745, 147
Royer, F., Gerbaldi, M., Faraggiana, R., & Gómez, A. E. 2002, A&A, 381, 105
Scowen, P. A., Gayley, K., Ignace, R., et al. 2022, Ap&SS, 367, 121
Seaton, M. J. 1979, MNRAS, 187, 73
Semaan, T., Hubert, A. M., Zorec, J., et al. 2018, A&A, 613, A70
Serkowski, K. 1973, in IAU Symp. 52, Interstellar Dust and Related Topics, ed. J. M. Greenberg & H. C. van de Hulst (Dordrecht: Reidel), 145
Serkowski, K., Mathewson, D. S., & Ford, V. L. 1975, ApJ, 196, 261
Shepard, K., Gies, D. R., Kaper, L., & De Koter, A. 2022, ApJ, 931, 35
Slettebak, A. 1975, ApJ, 197, 137
Spurr, R. J. D. 2006, JQSRT, 102, 316
Stetson, P. B. 1987, PASP, 99, 191
Tinney, C. G., Ryder, S. D., Ellis, S. C., et al. 2004, Proc. SPIE, 5492, 998
Townsend, R. H. D., Owocki, S. P., & Howarth, I. D. 2004, MNRAS, 350, 189
van Belle, G. T. 2012, A&ARv, 20, 51
van Leeuwen, F. 2007, A&A, 474, 653
Vandeportal, J., Bastien, P., Simon, A., Augereau, J.-C., & Storer, É. 2019, MNRAS, 483, 3510
Walker, G. A. H., Kuschnig, R., Matthews, J. M., et al. 2005, ApJL, 635, L77
Whittet, D. C. B., Martin, P. G., Hough, J. H., et al. 1992, ApJ, 386, 562
Wilking, B. A., Lebofsky, M. J., & Rieke, G. H. 1982, AJ, 87, 695
Wood, K., Bjorkman, K. S., & Bjorkman, J. E. 1997, ApJ, 477, 926
Zhao, M., Monnier, J. D., Pedretti, E., et al. 2009, ApJ, 701, 209
Zorec, J., Frémat, Y., Domiciano de Souza, A., et al. 2016, A&A, 595, A132